Shock Waves (2009) 19:151–162
DOI 10.1007/s00193-009-0197-7

ORIGINAL ARTICLE

Numerical simulation of H_2/air detonation using unstructured mesh

Fumiya Togashi · Rainald Löhner · Nobuyuki Tsuboi

Received: 29 October 2007 / Revised: 15 September 2008 / Accepted: 27 February 2009 / Published online: 31 March 2009

Abstract To explore the capability of unstructured mesh to simulate detonation wave propagation phenomena, numerical simulation of H_2/air detonation using unstructured mesh was conducted. The unstructured mesh has several advantages such as easy mesh adaptation and flexibility to the complicated configurations. To examine the resolution dependency of the unstructured mesh, several simulations varying the mesh size were conducted and compared with a computed result using a structured mesh. The results show that the unstructured mesh solution captures the detailed structure of detonation wave, as well as the structured mesh solution. To capture the detailed detonation cell structure, the unstructured mesh simulations required at least twice, ideally 5times the resolution of structured mesh solution.

Keywords Detonation · Unstructured mesh · CFD · H_2–air · Detailed chemical reaction model

PACS 47.40.Rs

1 Introduction

A detonation is a shock wave sustained by the energy released by combustion. For over 120 years, various experiments and calculations of this phenomenon have been done because the analysis of the nature and structure of a detonation is very significant from the point of safety engineering. These results, especially concerning the experimental data, are very useful even for the current study.

Recently, detonation has been applied to the next generation engines such as pulse detonation engine (PDE) and supersonic combustion Ram jet engine (SCRAM Jet) [1,2]. On the other hand, a detonation of the type considered here can also be applied to some fuel–air explosives. In order to understand the nature and structure of a detonation under these various situations, more analysis of a detonation under various circumstances is required. Especially, the development of proper numerical analysis tools is necessary to enhance understanding and reduce cost and risk. Numerical simulation of these flow fields is not an easy task because the computation includes complicated combustion kinetics, diffusion processes, and huge energy releases into the field and requires considerably more nodal points compared to inert compressible flow computations. The first numerical simulation of the detonation wave was performed by Taki and Fujiwara [3] for 2D detonation in oxyhydrogen mixture diluted by argon. Since then, the recent progress in both computational methods and available computer facilities makes the computation with detailed reaction models possible. Oran et al. [4] simulated reflected shock tube experiments in the weak and strong ignition regime in hydrogen–oxygen–argon mixtures using detailed 1D calculations in 1982 and performed 2D detonation simulations using detailed reaction models in 1998 [5]. MacCormack et al. [6] implemented the fully implicit, finite volume algorithm for 2D axisymmetric flows to a detailed H_2–air reaction for supersonic combustion phenomena in 1992. Tsuboi et al. [7,8] simulated 3D H_2–air detonation propagation in rectangular tube. They have also performed spin detonation propagation in rectangular tube

Communicated by F. Zhang.

F. Togashi (✉) · R. Löhner
College of Science, George Mason University,
4400 University Dr. MS 6A2, Fairfax, VA 22030, USA
e-mail: fumiya@togashi.us; fumiya.togashi@saic.com

N. Tsuboi
Institute of Space and Astronautical Science,
Japan Aerospace Exploration Agency, 3-1-1 Yoshinodai,
Sagamihara, Kanagawa 229-8510, Japan

and circular tube [9–12]. However those simulations are still limited to smaller spatial domains.

Currently, most of these computations have been conducted on structured and Cartesian meshes. The reason is that the analysis of the detonation phenomena requires higher order accuracy especially for capturing the detonation cell structures. Yang et al. [13] and Harris et al. [14] performed the numerical simulation for pulse detonation engine (PDE) using unstructured mesh. However, such a computation of estimating PDE's performance does not required very fine resolution like capturing the detonation cell structures. To the authors' knowledge the number of computations of capturing the detonation cell structure using unstructured mesh for is relatively small. However, unstructured mesh has the advantages of facilitating mesh refinement and flexibility for complicated configurations. Effective use of mesh refinement/coarsement can reduce the total CPU cost comparing with the uniform fine mesh. The coding of AMR to unstructured mesh is relatively easier than that of the Cartesian mesh. Several numerical simulations using unstructured mesh have been reported such advantages [15–17]. Besides, the less accuracy of unstructured mesh has been improving thanks to the tremendous efforts of lots of researchers in aerodynamics field [18,19]. Considering the future engineering requirement, establishment of numerical simulation on unstructured mesh will be useful for the future detonation research.

The motivation for this study is to construct a numerical investigation using unstructured meshes and to explore the capability of unstructured mesh approach for a numerical simulation of detonation wave phenomena. A mesh resolution study was conducted and the computed results are compared with corresponding structured mesh results and discussed with its verification and capability.

2 Reaction model and flow solver

2.1 Chemical reaction model and governing equations

The governing equations can be written as follows

$$\frac{\partial \mathbf{Q}}{\partial t}+\frac{\partial \mathbf{E}}{\partial x}+\frac{\partial \mathbf{F}}{\partial y}+\frac{\partial \mathbf{G}}{\partial z}=\mathbf{S} \tag{1}$$

$$\mathbf{Q}=\begin{bmatrix}\rho\\ \rho u\\ \rho v\\ \rho w\\ e\\ \rho_l\end{bmatrix},\quad \mathbf{E}=\begin{bmatrix}\rho u\\ \rho u^2+p\\ \rho uv\\ \rho uw\\ (e+p)u\\ \rho_l u\end{bmatrix},\quad \mathbf{F}=\begin{bmatrix}\rho v\\ \rho vu\\ \rho v^2+P\\ \rho vw\\ (e+p)v\\ \rho_l v\end{bmatrix},$$

$$\mathbf{G}=\begin{bmatrix}\rho w\\ \rho wu\\ \rho wv\\ \rho w^2+P\\ (e+p)w\\ \rho_l u\end{bmatrix},\quad \mathbf{S}=\begin{bmatrix}0\\0\\0\\0\\0\\ \omega_l\end{bmatrix} \tag{2}$$

where ρ is density, u, v, and w are velocities in the x, y, and z directions, e is total energy, ρ_l is density of lth species, and P is pressure.

The total energy is defined as follows

$$e=\sum_{s=l}^{Ns}\rho_s h_s-p+\frac{\rho}{2}\left(u^2+v^2+w^2\right) \tag{3}$$

where N_s is total number of species. The thermal equation of state for a perfect gas is given by $P=\sum_{s=l}^{Ns}\rho_s R_s T$, where R_s denotes the gas constant for each species. The specific heat at constant pressure for each species, C_{ps}, which is used to evaluate the total energy through the specific enthalpy

$$h_s=h_s^0+\int_{\mathrm{Tref}}^{T} C_{ps}\mathrm{d}T \tag{4}$$

is given as

$$C_{ps}=\frac{R}{M_s}\left(a_{1,s}+a_{2,s}T+a_{3,s}T^2+a_{4,s}T^3+a_{5,s}T^4\right) \tag{5}$$

The coefficients in (5) are obtained from the data in the JANAF tables [20].

In this study, the Petersen and Hanson model (PH model) is used for chemical kinetics that consists of 9 species (H_2, O_2, H, O, OH, HO_2, H_2O_2, H_2O, and N_2) and 18 elementary reactions. The data for the chemical reaction was taken from the paper of Petersen and Hanson [21], and is reproduced in detail in Appendix. This model was proposed by Petersen and Hanson as a new detailed chemical reaction model to solve detonation problems. The model has the feature that the pressure dependence on a forward reaction coefficient is included in the collision reaction with a third body. Namely, HO_2 and H_2O_2 chemistry near the second and third explosion limits are introduced that are necessary for ignition at extremely high pressure but are lacking for some finite rate chemical models currently in use. The production rate of each chemical species, $\dot{\omega}_s$ is given by combining the elementary chemical reactions in the kinetic model as follows

$$\dot{\omega}_s=M_s\sum_{j=1}^{N_r}\left(\sum_{l=1}^{n}\alpha_{lj}C_l\right)^{\beta_j}\left(\gamma''_{js}-\gamma'_{js}\right)\times\left[K_{fj}\prod_{i=1}^{N_s}C_i^{\gamma'_{ji}}-K_{bj}\prod_{i=1}^{N_s}C_i^{\gamma''_{ji}}\right] \tag{6}$$

where M_s denotes the molecular weight of species s, C_s denotes the mole fraction, α is a third body coefficient, and

γ''_{js} and γ'_{js} are the stoichiometric coefficients. K_f and K_b are the forward and backward rate constants derived from an Arrhenius form as follows

$$K(T) = A\exp(-E/RT) \tag{7}$$

The governing equations are the Euler equations and solved by an explicit method. The three stage Runge–Kutta method is used for temporal accuracy for 3.0 and 5.0 μm meshes. We tested temporal first-order and third-order Runge–Kutta for 2.5 micron mesh. There were almost no differences between these two computed results because of highly fine mesh resolution. So the temporal accuracy for 2.5 μm and finer resolution is temporal first-order scheme to save CPU time. As an approximate Rieman solver, the HLLC scheme is employed. High-order flux reconstruction is carried out via a MUSCL scheme. The source term of the chemical reaction was treated in a linearly point-implicit manner.

2.2 3D flow solver

The chemical reaction model described above was implemented into our in-house code, FEFLO, a general-purpose CFD code based on the following general principles

- Use of unstructured grids (automatic grid generation and mesh refinement);
- Finite element discretization of space;
- Separate flow modules for compressible and incompressible flows;
- ALE formulation for body fitted moving grids;
- Embedded formulation for complex/dirty geometries;
- Edge-based data structures for speed;
- Optimal data structures for different supercomputer architectures;
- Bottom-up coding from the subroutine level to assure an open-ended,

The code has a long history of relevant applications [22–30]. Over the last 3 years, FEFLO has been ported to both shared memory [31–33] and distributed memory [24,34], and [35] machines.

The spatial approximation is accomplished via the Galerkin weighted residual method. The unknown vector $\mathbf{u}$ is approximated by a set of shape-functions

$$\mathbf{u} \approx N^i \mathbf{u}_i^h \tag{8}$$

where N^i denotes the shape function associated with node i and $\mathbf{u}_i^h$ the numerical value of $\mathbf{u}$ at node i. Weighing (8) with the available set of shape-function N^i leads to

$$\int_\Omega N^i(\mathbf{u}^h_{,t} + \nabla\cdot\mathbf{F})\mathrm{d}\Omega = 0$$

$$\Rightarrow \int_\Omega N^i[N^i(\hat{\mathbf{u}}_j)_{,t} + \nabla\cdot\mathbf{F}(N^i\hat{\mathbf{u}}_j)]\mathrm{d}\Omega = 0 \tag{9}$$

In order to simplify the algebra (and CPU) involved, one may use, without noticeable deterioration of results

$$\mathbf{F}(N^j\hat{\mathbf{u}}_j) = N^j\mathbf{F}(\hat{\mathbf{u}}_j) \tag{10}$$

which then translates into

$$\int_\Omega N^i N^j \mathrm{d}\Omega(\hat{\mathbf{u}}_\mathbf{j})_{,t} + \int_\Omega N^i\nabla\cdot N^j\mathrm{d}\Omega\mathbf{F}(\hat{\mathbf{u}}_\mathbf{j}) = 0 \tag{11}$$

or

$$\mathbf{M}_c\cdot\hat{\mathbf{u}}_{,t} = \mathbf{r}, \quad \mathbf{r} = \mathbf{r}(\mathbf{u}) \tag{12}$$

Obviously, integration by parts is possible for (12). For linear elements, one can show that this is equivalent to a finite volume method. All appearing integrals are evaluated using the element subdomain paradigm

$$\int_\Omega \cdot\cdot = \sum_{\mathrm{el}}\int_{\Omega_{\mathrm{el}}} \cdot\cdot \tag{13}$$

For linear elements, it is advantageous to convert the element-based evaluations of (12) into an edge-based loop of the form:

$$\mathbf{r}^j = d_k^{ij}\left(\mathbf{F}_j^k + \mathbf{F}_i^k\right) \tag{14}$$

where d_k^{ij} contains all the geometric parameters associated with the elements surrounding the edge $\boldsymbol{i}, \boldsymbol{j}$ and the dimension $\boldsymbol{k}$. The inner product over the dimensions k may be written in compact form as

$$r^i = D^{ij}F_{ij} = D^{ij}\left(f_i + f_j\right) \tag{15}$$

where the f_i are the 'fluxes along edges', obtained from the scalar product

$$f_i = S_k^{ij}\mathbf{F}_i^k, \quad S_k^{ij} = \frac{d_k^{ij}}{D^{ij}}, \quad D^{ij} = \sqrt{d_k^{ij}d_k^{ij}} \tag{16}$$

For the standard Galerkin approximation we have

$$F_{ij} = f_i + f_j \tag{17}$$

Comparing this expression to a 1D analysis, we see that it corresponds to a central difference approximation of the first-order derivative fluxes. This flux is replaced by the consistent numerical flux described in the previous section.

The extrapolation to neighboring values required for limiting is accomplished by evaluating the gradients at the nodes [36].

3 Computational conditions and meshes

3.1 Computational conditions

The computations modeled a detonation propagating in a stoichiometric H_2–O_2 gas, diluted with N_2. The mole concentration ratio of the $H_2/O_2/N_2$ gas mixture was 2:1:3.76, initial pressure was 1 atm, and temperature was 300 K. At first, the 1D detonation wave was initiated and allowed to propagate until it reached CJ velocity. Then the 1D computed result was placed on a 2D grid with a sheet of unburned gas mixture behind the detonation front and also let propagate until it formed the cell structures [37]. The tube width of all computations in this study is 1 mm.

To compare the computed results for a resolution study, the numerical simulation using structured mesh was also conducted. The governing equations are same as the computation using unstructured mesh. A second-order Harten–Yee non-MUSCL type TVD scheme is used for the numerical flux in the convective terms [38]. The averaged state on a computational cell boundary is given by the generalized Roe's average [39] to evaluate the numerical flux in the convective terms. The chemical reaction model is the Petersen and Hanson model that is same as the computation of unstructured mesh.

3.2 Computational meshes

Powers et al. [40,41] reported the guidelines concerning with the resolution requirement in complex chemistry simulations. Reference [40] mentioned that the element size of 0.1 μm is required as the finest length scales for the CJ H_2–air detonation wave at 1 atm and 298 K. This length is roughly three orders of magnitude finer than the induction zone thickness. However, it is very difficult to apply this scale to 2D simulations under current computational sources. Considering the available computational sources and employing the Euler equations, we applied 5 μm element size for structured mesh in this study. The mesh size of 5 μm gives a resolution of 32 nodal points in the theoretical half reaction length [42] which equals 160 μm for H_2 at atmospheric pressure [43]. A series of unstructured mesh is prepared for resolution study. The average element size is 1.0, 2.5, 3.0, and 5.0 μm, respectively. Each domain of the unstructured mesh has a 2–3 element thickness. Figure 1 shows the unstructured mesh configure used in this study. The computational meshes are composed of all tetrahedral. To prevent less accuracy of computation, all tetrahedral are preferred to be equilateral. So the mesh quality was checked after generating a computational mesh and re-generated if necessary. The AMR is applied to 1.0 μm mesh. The domain range $x = 0$–1.5 mm has 2.0 μm resolution and the domain $x = 1.5$–4.0 mm has 1.0 μm resolution. Generally, the unstructured mesh method is more diffusive than the structured mesh scheme. The unstructured mesh system required all the adjacent cell information to obtain the gradient of physical values three dimensionally (x, y, and the physical value) even on the 2D computation. So the gradient on the unstructured mesh is less accuracy especially on the region where the physical values varies drastically comparing with the structured mesh system which can achieve the higher accuracy one dimensionally even on 3D configuration. Some papers investigated and reported this issue [44,45]. Considering the very strong shock phenomena such as detonation waves, finer resolution will be required for the unstructured mesh system. Aftosmis et al. [51] reported that the distorted triangle mesh gives less accuracy comparing with the equilateral triangle mesh. The distorted tetrahedral mesh could give poor results even if using sufficiently finer mesh.

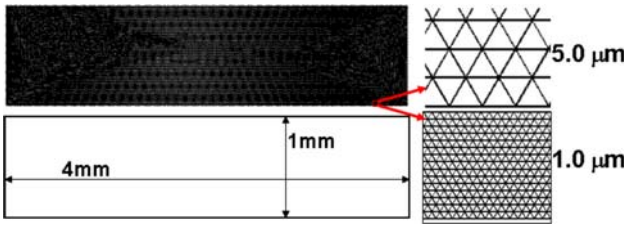

Fig. 1 Unstructured meshes. *Top* Average element size 5.0 μm, *bottom* average element size 1.0 μm)

4 Results and discussion

4.1 Chemical reaction model verification

To verify the implemented chemical reaction model, 0D homogeneous ignition simulations were performed. Figure 2 shows the mole fraction history at 1,000 K and 1 atm. The second explosion limit appears when temperature decreases with pressure of 1 atm. This limit is governed by the balance of chain branching and termination of $H + O_2 = OH + O$ and $H + O_2 + M = HO_2 + M$. Chemical behavior in the second explosion limit is well known by the experimental data and most of the chemical reaction models include its limit. The PH model implemented also shows that H and OH increase exponentially and HO_2 becomes a constant value close to the ignition time at 2.3×10^{-4} s. Figure 3 shows the ignition delay comparison between the CFD codes and CHEMKIN. The chemical reaction model used in this study was Petersen and Hanson model [21]. The ignition time in this study was defined as the moment when the rate of temperature increase became the maximum. The computed results by CFD codes agreed well with the results by CHEMKIN. The computed results between the unstructured code and the structured code also show good agreement, so the unstructured code and the

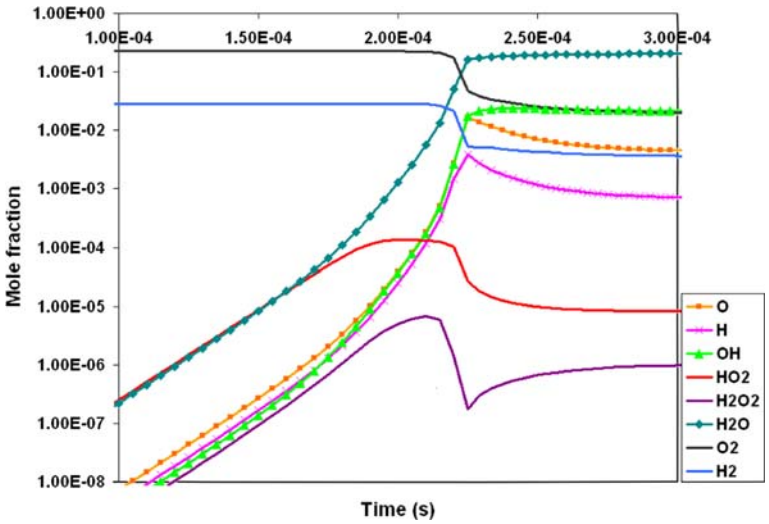

Fig. 2 Species mole fraction at 0D homogeneous ignition simulations

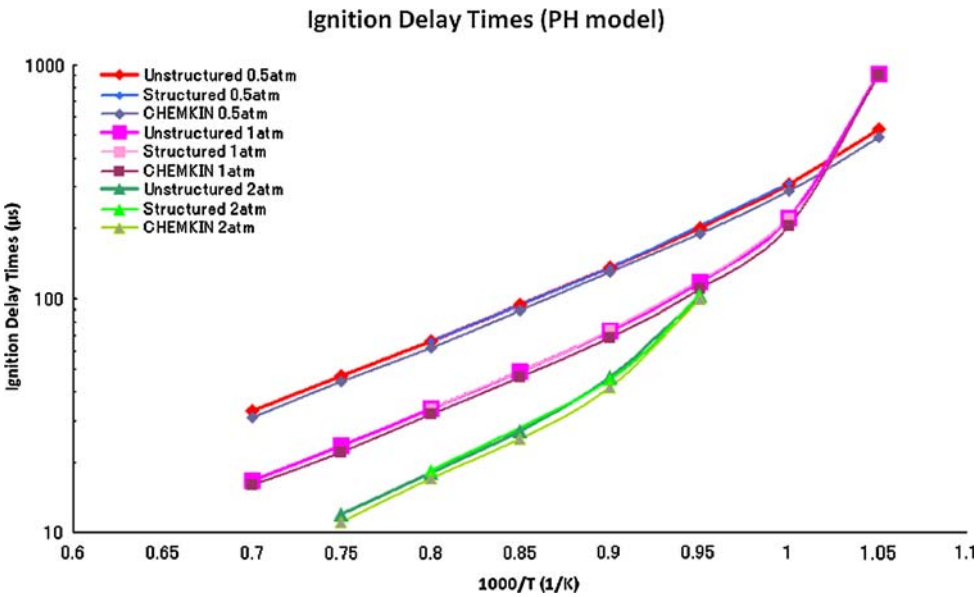

Fig. 3 Ignition delay comparison between CFD code and CHEMKIN

structured code have a same accuracy for the chemical reaction computation.

4.2 Instantaneous computed contours

Figures 4, 5, and 6 show the computed contours of pressure, OH mass fraction, and H_2 mass fraction with different computational mesh sizes, respectively. The simulation for average element size of 1.0 μm required about 100 h on 16 processors of SGI ALTIX 4700. On the other hand, simulation for average element size of 5.0 μm required about 10 h on the same computational source. The CFL number for all computations is 0.9, average time step is about 7×10^{-10} s for 1.0 μm resolution and 3×10^{-9} s for 5.0 μm resolution. The numerical error in species concentrations is 0.8% at maximum even for 5.0 μm resolution because the continuity equation for total density and that for species densities are solved simultaneously.

The computed results using 1.0, 2.5, and 3μm elements captured a triple point clearly. Especially, the computation of 1.0 and 2.5 μm element resolution captured the "keystone" features of the detonation [46] as much as the computation using structured mesh in Fig. 5. On the other hand, the computation with average 5 μm elements managed to capture the triple point from the pressure contours, however, the computed contours of OH mass fraction and H_2 mass fraction could not capture the phenomenon clearly. This instability is caused by the coarse mesh resolution. Many researchers

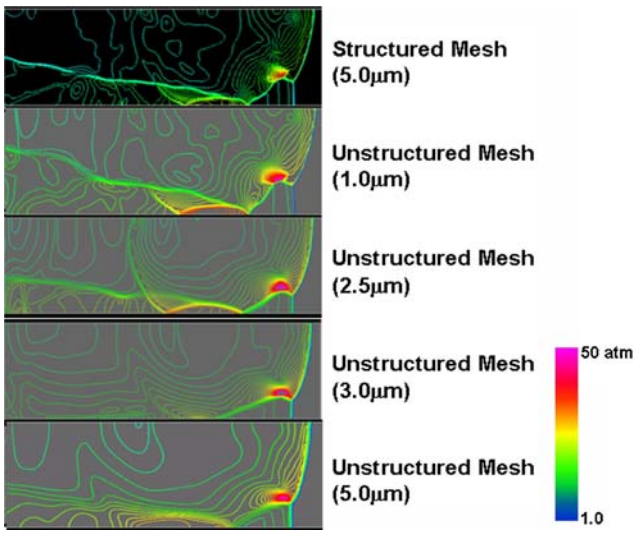

Fig. 4 Computed pressure contours using structured mesh and unstructured mesh with different size of average mesh elements. (average element size is 1.0, 2.5, 3.0, and 5.0 μm, respectively)

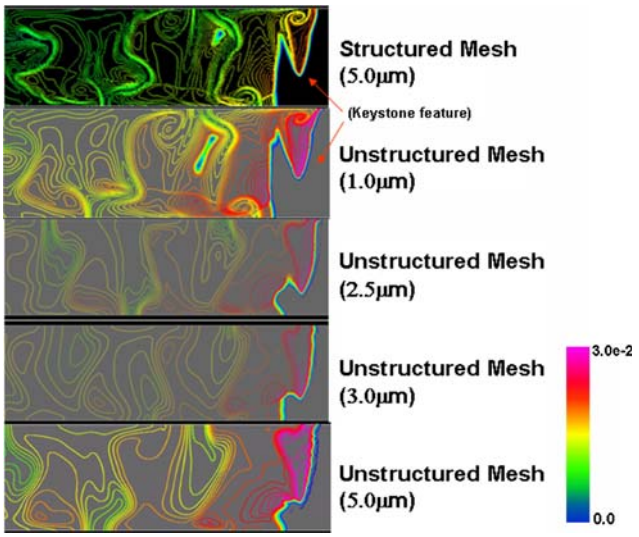

Fig. 5 Computed instantaneous mass fraction of OH contours with different size of average mesh elements

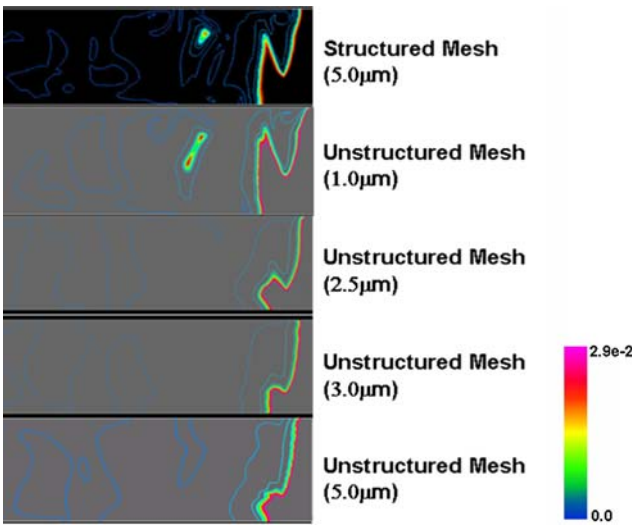

Fig. 6 Computed instantaneous mass fraction of H_2 contours with different size of average mesh elements

have been reported that detonation cell size is significantly dependent on grid spacing, and poor resolution causes small cell size [47].

4.3 Maximum pressure histories and instantaneous pressure profiles

Figure 7 shows computed maximum pressure histories with different size of average mesh elements. The computed results with average 1.0, 2.5, and 3 μm elements show similar results with the results for the structured mesh in Fig. 8. However the computation with average 5 μm elements formed its cell structure temporally but could not sustain the cell structure and become a plane detonation wave during its propagation.

To study the effect of the mesh resolution on the maximum pressure histories in detail, the comparison of the instantaneous pressure values on the upper/lower wall boundaries was conducted. Figure 9 shows the comparison of the instantaneous pressure values on the upper/lower wall boundaries between the unstructured mesh and the structured mesh at the time which is identical to Figs. 4, 5 and 6. In Fig. 9, (lower wall), the transverse wave captured on the 1.0 μm unstructured mesh at $x = 2.6 \times 10^{-1}$ cm is slightly strong comparing with the structured mesh computation, while the transverse wave captured on the 3.0 μm unstructured mesh at $x = 2.6 \times 10^{-1}$ cm is relatively unclear comparing with the 1.0 μm unstructured mesh result and structured mesh result. The result on the 5.0 μm unstructured mesh is more unresolved especially at $x = 2.6 \times 10^{-1}$ cm. These differences of capturing the transverse wave resulted in the different structure of shock waves around the gas pocket structures and caused the different shape of the gas pocket shape as shown in Figs. 5 and 6. The pressure values of the detonation front on the lower and upper walls are well agreed between the 1.0 μm unstructured and the structured mesh results as shown in Fig. 9. The pressure value of the detonation front on the lower wall boundary on 3.0 μm unstructured mesh is also agreed with the 1.0 μm unstructured and the structured mesh results, however, the pressure values around the transverse wave at $x = 2.6 \times 10^{-1}$ cm on the lower wall is relatively unresolved as described above. Figure 10 shows the time to pressure history on the lower boundary of the computational domain. The pressure peak values and the pressure peak intervals are well agreed between the 1.0 μm unstructured and the structured mesh results.

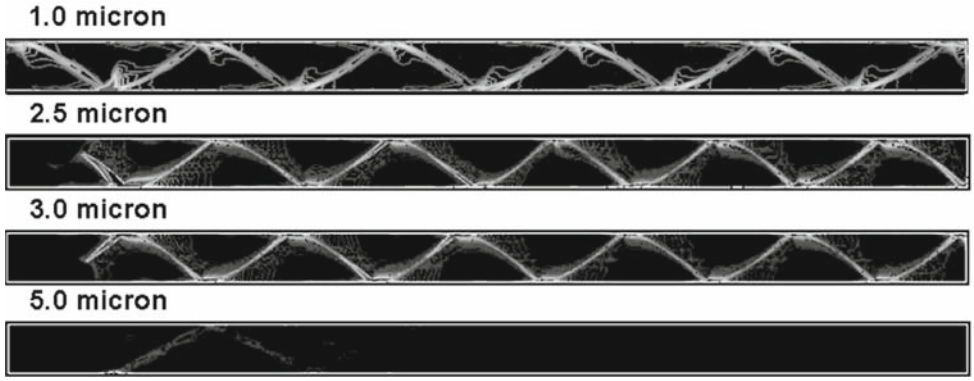

Fig. 7 Computed maximum pressure histories with different size of average mesh elements. (The average element size is 1.0, 2.5, 3.0, and 5.0 μm, respectively. Plot range: 30–70 atm)

Fig. 8 Computed maximum pressure history for structured mesh (range 30–70 atm)

Fig. 9 Comparison of instantaneous pressure values on upper/lower wall boundary between the unstructured mesh and the structured mesh

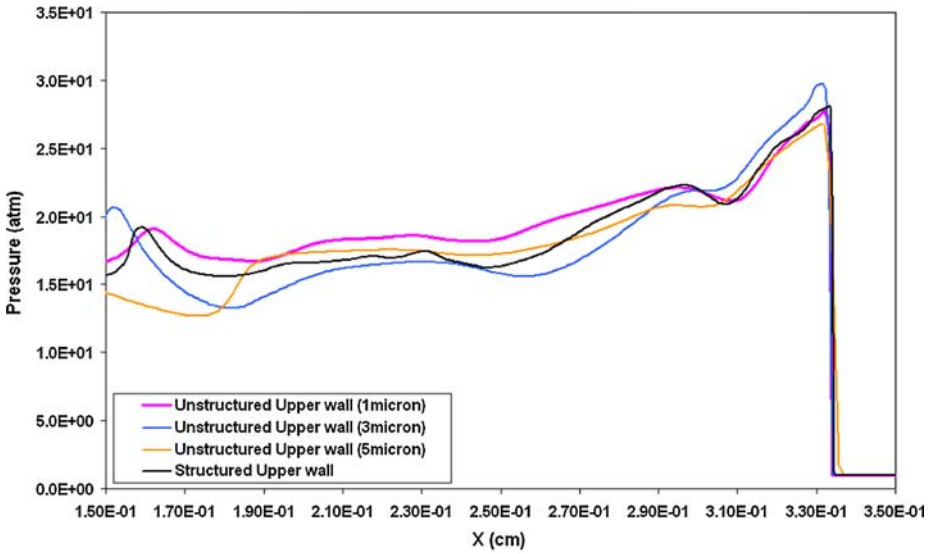

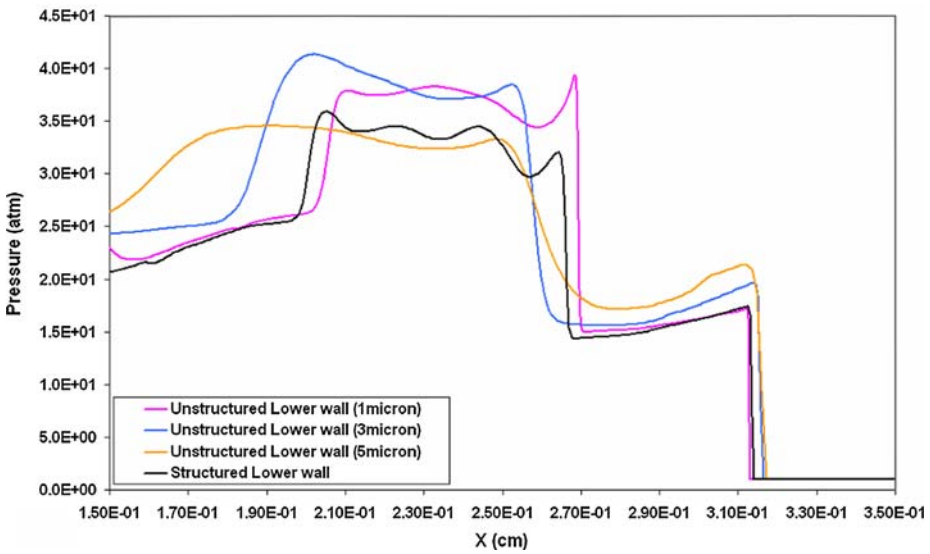

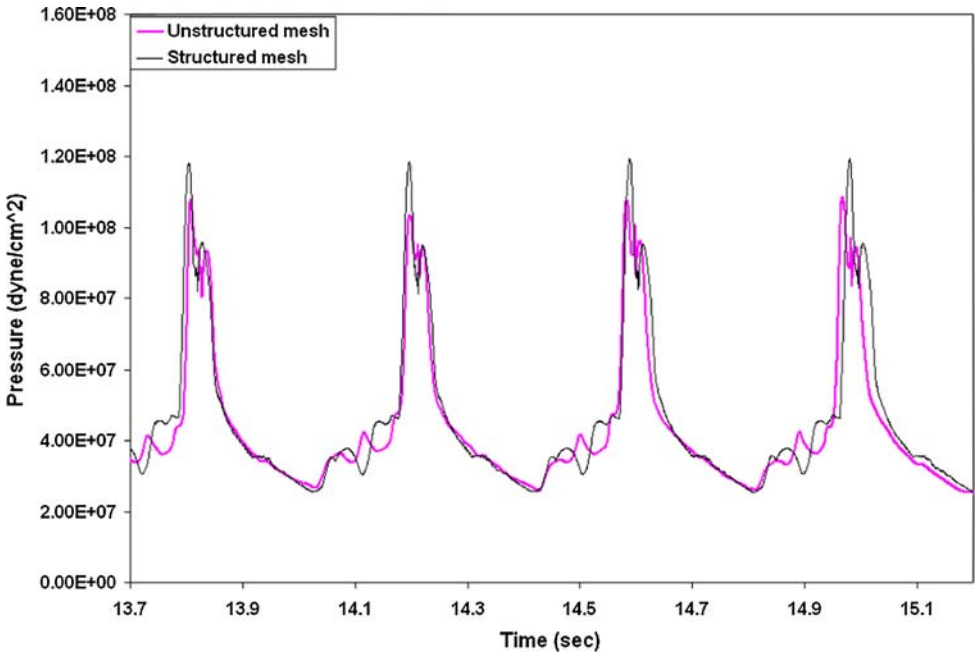

Fig. 10 Comparison of pressure histories on wall boundary between the 1.0 μm unstructured mesh and the structured mesh

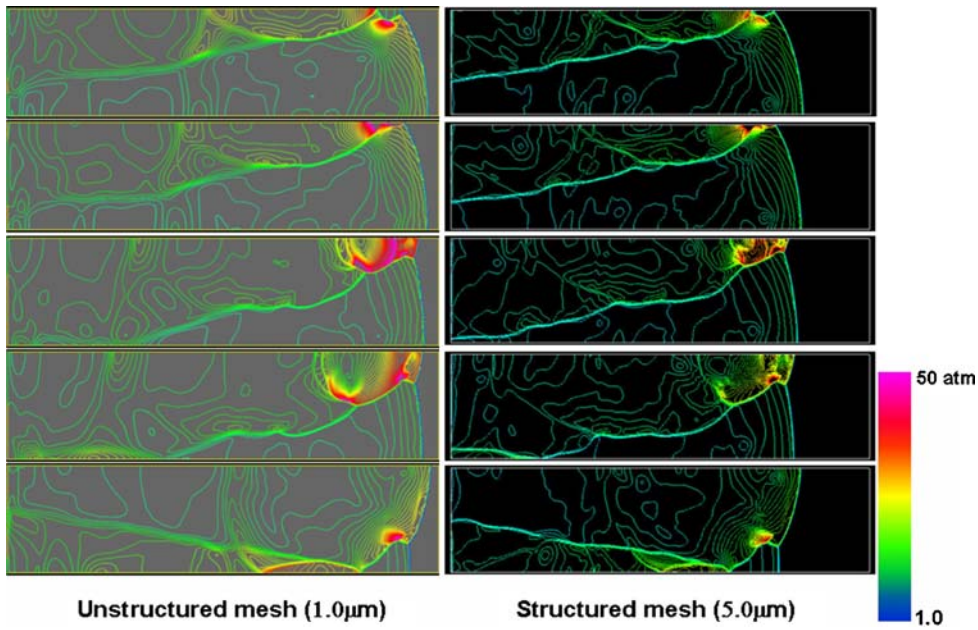

Fig. 11 Comparison of computed instantaneous pressure contours between unstructured mesh and structured mesh

4.4 Keystone and unburned gas pocket

The formation of unburned pocket behind the detonation front has been numerically studied by Oran et al. [5,48]. Gamezo et al. [49] reported that unburned pockets are commonly observed. A recent advanced experimental technique such as the method of planar laser induced predissociated fluorescence (LIPF) has enabled Pintgen et al. [46] to visualize the OH concentration behind the detonation front. They obtained images of the creation of a keystone-shaped region behind the detonation front, and they also showed that no unburned pockets could be observed. The effect of the mesh resolution on the unburned gas pocket depends not only on the resolution around the detonation front but also on the resolution around the shear layer behind the detonation front. We discussed the resolution around the shear layer on the next section.

Figures 11, 12, and 13 show the comparisons of computed instantaneous contours using the structured mesh and the unstructured meshes. The average element size of unstructured

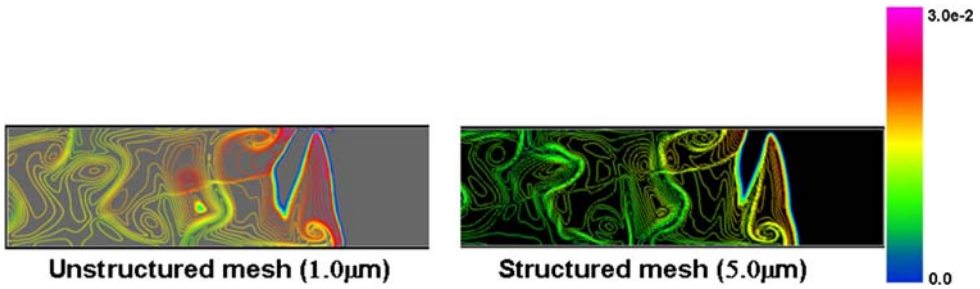

Fig. 12 Comparison of computed instantaneous OH mass fraction contours between unstructured mesh and structured mesh

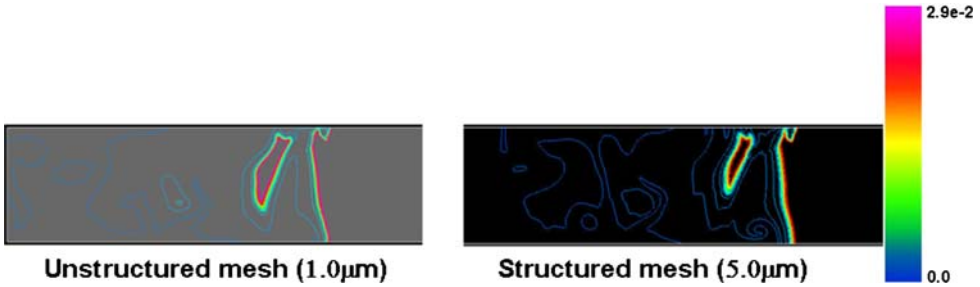

Fig. 13 Comparison of computed instantaneous H_2 mass fraction contours between unstructured mesh and structured mesh

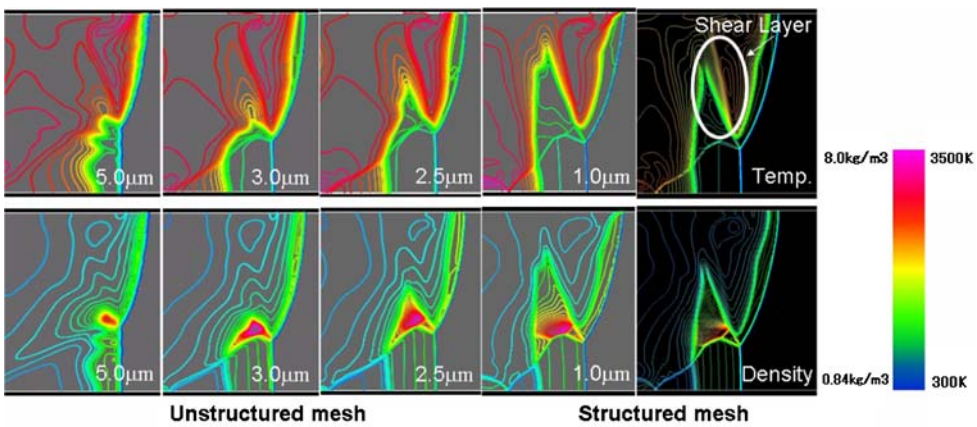

Fig. 14 Comparison of computed instantaneous temperature and density contours between unstructured mesh and structured mesh

mesh is 1.0 μm and that of structured mesh is 5 μm. The computed results using unstructured mesh and structured mesh show the "keystone" feature and unburned gas pocket behind the detonation front as shown in Figs. 12 and 13, respectively. The unstructured mesh results using 2.5 μm element size and more could not capture the vortices behind the mach stem. The average element size of 1.0 μm could manage to capture them like 5 μm structured mesh did.

4.5 Shear layer

To study the effect of the mesh resolution of the unstructured mesh on the unburned gas pocket, the comparison of the shear layer behind the detonation front was conducted as shown in Fig. 14.The comparison of the ignition delay time shows that the unstructured code and the structured code have almost same accuracy of the chemical reaction as shown in Fig. 3. So the difference of the unburned gas pocket shape might be caused by the resolution for the fluid phenomena such as shock wave structure and shear layer. Figure 14 shows the enlarged view of temperature and density contours at the time which is identical to Figs. 4, 5 and 6. The shear layer around the key stone features on the unstructured mesh is slightly unclear comparing with the structured mesh system even on 1.0 μm mesh resolution as shown clearer in the temperature contours of Fig. 14. Considering these shear layer comparison and the comparison of the instantaneous pressure values in Fig. 9, this less accuracy of capturing the detailed shock

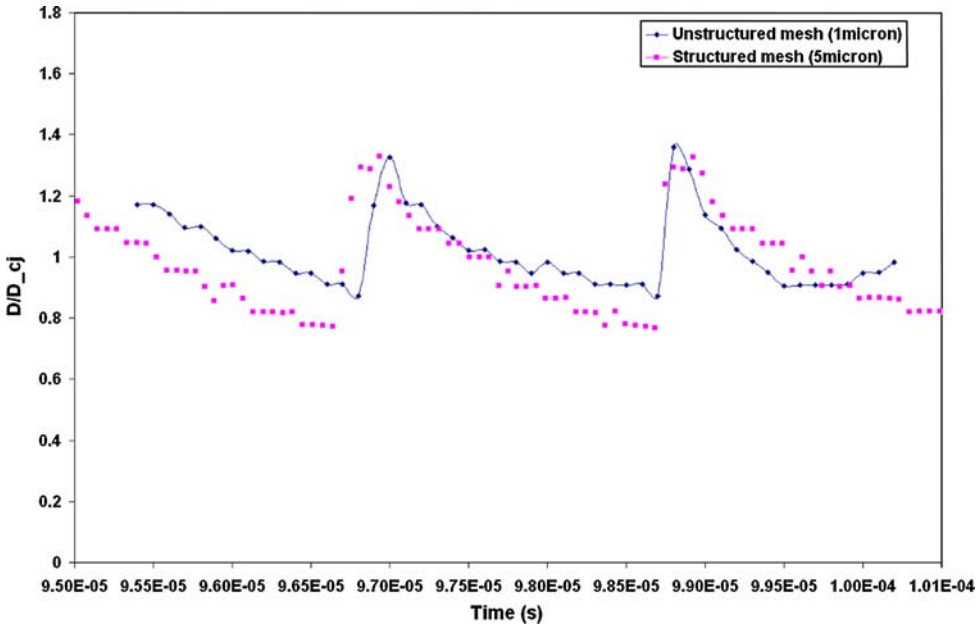

Fig. 15 Comparison of instantaneous detonation wave velocity between unstructured mesh result and structured mesh result at each time

structure around the transverse wave could also cause the difference of the shock structure around the key stone features and result in the gas pocket shape difference between the two mesh systems.

4.6 Detonation velocity

The detonation velocity was calculated in order to confirm the C–J velocity in the simulation. Figure 15 shows the history of the instantaneous detonation velocity of the computation using 1.0 μm unstructured mesh and 5.0 μm structured mesh. In both computations, the detonation velocity varies at 0.8–1.4 $D/D_{\_CJ}$ and shows similar variation.

Thus far we can simulate the detonation cell structure such as triple point and keystone feature by using unstructured mesh.

4.7 Advantage of the unstructured mesh system

Obviously the structured mesh system has an advantage of spacious and temporal accuracy for simple domains such as straight tube/cylinder and so on. However, the unstructured mesh system has an advantage of the easy application of AMR [15] because the unstructured mesh system allows adding/removing nodal points without modifying the code drastically. It can make the computation of spherical detonation or bent tube propagation. The numerical simulation of spherical detonation, for example, requires tremendous nodal points as reported by Watt et al. [50]. They mentioned the computation using sufficiently high resolution of structured mesh to obtain reliable results for spherical detonation would be almost impossible even for 2D computation. The unstructured mesh system with AMR can be a powerful tool for this kind of problems. The problem of less accuracy of the unstructured mesh system has been improved by various approaches such as discontinuous Galerkin method. Applying such a higher order scheme for the unstructured mesh system will make it practical to the application to the numerical simulation of detonation wave structure in complicated configures or expanding detonation waves.

5 Conclusions

Numerical simulation of H_2/air detonation using unstructured mesh was conducted. To examine the resolution dependency of the unstructured mesh, several different mesh size simulations were conducted and compared with the results from the structured mesh simulation.

The results show that unstructured mesh simulation conducted with the identical mesh resolution of structured mesh study, could not capture the detailed detonation cell structure. However, unstructured mesh with about twice the resolution could capture the detailed features of the detonation wave, such as the triple point and the keystone feature. However, to capture the vortices behind the Mach stem, unstructured mesh required about five times resolution. The mesh quality is also very important factor for the unstructured system.

We conclude that the numerical simulation using unstructured mesh could obtain physically meaningful results using at least twice the resolution, ideally five times the resolution of the structured mesh resolution.

Appendix

No.	Reaction	A	n	E	Comments
1.	$O + H_2 = H + OH$	5.00×10^4	2.70	6, 290	
2.	$H + O_2 + M = HO_2 + M$	2.80×10^{18}	−0.90	0	c
3.	$H + O_2 + O_2 = HO_2 + O_2$	3.00×10^{20}	−1.70	0	
4.	$H + O_2 + H_2O = HO_2 + H_2O$	9.38×10^{18}	−0.80	0	
5.	$H + O_2 + N_2 = HO_2 + N_2$	2.60×10^{19}	−1.20	0	
6.	$H + O_2 = O + OH$	8.30×10^{13}	0.00	14, 413	
7.	$H + HO_2 = O_2 + H_2$	2.80×10^{13}	0.00	1, 068	
8.	$H + HO_2 = OH + OH$	1.34×10^{14}	0.00	635	
9.	$H + H_2O_2 = HO_2 + H_2$	1.21×10^7	2.00	5, 200	
10.	$OH + H_2 = H_2O + H$	2.16×10^8	1.50	3, 430	
11.	$OH + OH + M = H_2O_2 + M$	7.40×10^{13}	−0.40	0	k_{inf}, d,e
		2.30×10^{18}	−0.90	−1,700	k_0
12.	$OH + HO_2 = O_2 + H_2O$	2.90×10^{13}	0.00	−500	
13.	$OH + H_2O_2 = HO_2 + H_2O$	1.75×10^{12}	0.00	320	k_a, f
		5.80×10^{14}	0.00	9,560	k_b, f
14.	$HO_2 + HO_2 = O_2 + H_2O_2$	1.30×10^{11}	0.00	−1,630	k_c, g
		4.20×10^{14}	0.00	12,000	k_d, g
15.	$O + O + M = O_2 + M$	1.20×10^{17}	−1.00	0	h
16.	$O + H + M = OH + M$	5.00×10^{17}	−1.00	0	d
17.	$H + OH + M = H_2O + M$	2.20×10^{22}	−2.00	0	i
18.	$H + H + M = H_2 + M$	1.00×10^{18}	−1.00	0	j

a. All reactions are reversible.
b. $k(T) = AT^n \exp(-E/RT)$: units are in cal. mol, cm^3, and s.
c. M does not include O_2, H_2O, or N_2; all collision efficiencies = 1, 0
d. Collision efficiencies for M; $N_2 = 1.0$, $H_2 = 2.0$, $H_2O = 6.0$, and Ar = 0.70, all others = 1.0
e. $k_{inf} = k_\infty [P_r/(1 + P_r)]F$, $P_r = \frac{k_0[M]}{k_\infty}$, The factor F is prescribed by the method of Troe, $\ln F = \left\{1 + \left[\frac{\ln P_r + c}{n - d(\ln P_r + c)}\right]^2\right\}^{-1} \ln F_c$, where $c = -0.4 - 0.67 \ln(F_c)$, n =0.75−1.27 $\ln(F_c)$, d = 0.14, and The Troe centering parameter, F_c is, $F_c = (1-a)\exp(-T/T^{***}) + a\exp(-T/T^*) + \exp(-T^{**}/T)$ where $a = 0.7346$, $T^{***} = 94$, $T^* = 1,756$, $T^{**} = 5,182$
f. Rate coefficient is non-Arrhenius; $k_{13} = k_a + k_b$
g. Rate coefficient is non-Arrhenius; $k_{14} = k_c + k_d$
h. Collision efficiencies for M; $N_2 = 1.0$, $H_2 = 2.4$, $H_2O = 15.4$, and Ar = 0.83, all others = 1.0
i. Collision efficiencies for M; $N_2 = 1.0$, $H_2 = 0.73$, $H_2O = 3.65$, and Ar = 0.38, all others = 1.0
j. Collision efficiencies for M; $N_2 = 1.0$, $H_2 = 1.7$, $H_2O = 7.0$, and Ar = 0.63, all others = 1.0

References

1. Kailasanath, K.: Review of propulsion applications of detonation waves. AIAA J. **38**(9), 1698–1708 (2000). doi:10.2514/2.1156
2. Henry, J.R., Anderson, G.Y.: Design considerations for the air flame integrated Scramjet, NASA TM X2895 (1973)
3. Taki, S., Fujiwara, T.: Numerical analysis of two-dimensional non-steady detonations. AIAA J. **16**, 73–77 (1978). doi:10.2514/3.60859
4. Oran, E.S., Young, T.R., Boris, J.P.: Weak and strong ignition. I. Numerical simulations of shock tube experiments. Combust. Flame **48**, 135–148 (1982). doi:10.1016/0010-2180(82)90123-7
5. Oran, E.S., Weber, J.W. Jr., Stefaniw, E.I., Lefebvre, M.H., Anderson, J.D. Jr.: A numerical study of a two-dimensional H_2–O_2–Ar detonation using a detailed chemical reaction model. Combust. Flame **113**, 147–163 (1998). doi:10.1016/S0010-2180(97)00218-6
6. Wilson, G.J., MacCormack, R.W.: Modeling supersonic combustion using a fully implicit numerical method. AIAA J. **30**(4), 1008–1015 (1992). doi:10.2514/3.11021
7. Tsuboi, N., Katoh, S., Hayashi, A.K.: Three-dimensional numerical simulation for hydrogen/air detonation: rectangular and diagonal structures. Proc. Combust. Inst. **29**, 2783–2788 (2002). doi:10.1016/S1540-7489(02)80339-X
8. Eto, K., Tsuboi, N., Hayashi, A.K.: Numerical study on three-dimensional C–J detonation waves: detailed propagating mechanism and existence of OH radical. In: Proceedings of the Combustion Institute, vol. 30, pp. 1907–1913. The Combustion Institute, USA (2005)
9. Tsuboi, N., Eto, K., Hayashi, A.K.: Three-dimensional numerical simulation of H_2/air detonation in a circular tube: structure of spinning mode. In: 20th International Colloquium on the Dynamics of Explosions and Reactive Systems, vol. 71, Montreal, Canada, July 2005
10. Hayashi, A.K., Eto, K., Tsuboi, N.: Numerical simulation of spin detonation in square tube. In: 20th International Colloquium on the Dynamics of Explosions and Reactive Systems, vol. 85, Montreal, Canada, July 2005
11. Tsuboi, N., Hayashi, A.K.: Numerical study on spinning detonations. In: 31st International Symposium on Combustion, pp. 2389–2396 (2007)
12. Tsuboi, N., Eto, K., Hayashi, A.K.: Detailed structure of spinning detonation in a circular tube. Combust. Flame **149**(1/2), 144–161 (2007). doi:10.1016/j.combustflame.2006.12.004
13. Ma, F., Choi, J.Y., Yang, V.: Thrust chamber dynamics and propulsive performance of single-tube pulse detonation engines. J. Propuls. Power **21**(3), 512–526 (2005). doi:10.2514/1.7393
14. Harris, P.G., Stowe, R.A., Ripley, R.C., Guzik, S.M.: Pulse detonation engine as a Ramjet replacement. J. Propuls. Power **22**(2), 462–473 (2006). doi:10.2514/1.15414
15. Loth, E., Sivier, S., Baum, J.: Adaptive unstructured finite element method for two-dimensinal detonation simulations. Shock Waves **8**(1), 47–53 (1998)
16. Gessner, T.: Time-dependent adaption for supersonic combustion waves modeled with detailed reaction mechanisms, PhD thesis, University of Freiburg (2001)
17. Pimentel, C., Azevedo, J., Silva, L.: Numerical study of wedge supported oblique shock wave-oblique detonation wave transitions.

J. Braz. Soc. Mech. Sci. **24**, 149–157 (2002). doi:10.1590/S0100-73862002000300002
18. Luo, H., Baum, J., Lohner, R.: A Hermite WENO-based limiter for discontinuous Galerkin method on unstructured grids, AIAA 2007-0510 (2007)
19. Wang, Z.J.: Spectral (finite) volume method for conservation laws on unstructured grids: basic formulation. J. Comput. Phys. **178**, 210–251 (2002). doi:10.1006/jcph.2002.7041
20. Stull, D., Prophet, H.: JANAF Thermochemical Tables, 2nd edn. NSRDS-NBS37 (1971)
21. Petersen, E.L., Hanson, R.K.: Reduced kinetics mechanisms for Ram accelerator combustion. J. Propuls. Power **15**(4), 591–600 (1999). doi:10.2514/2.5468
22. Baum, J.D., Löhner, R.: Numerical simulation of shock interaction with a modern main battle field tank, AIAA-91-1666 (1991)
23. Baum, J.D., Luo, H., Löhner, R.: Numerical simulation of a blast inside a boeing 747, AIAA-93-3091 (1993)
24. Ramamurti, R., Löhner, R.: Simulation of flow past complex geometries using a parallel implicit incompressible flow solver. In: Proceedings of 11th AIAA CFD Conference, pp. 1049, 1050, Orlando (1993)
25. Baum, J.D., Luo, H., Löhner, R.: A new ALE adaptive unstructured methodology for the simulation of moving bodies, AIAA-94-0414
26. Baum, J.D., Luo, H., Löhner, R.: Numerical simulation of blast in the world trade center, AIAA-95-0085 (1995)
27. Baum, J.D., Luo, H., Löhner, R., Yang, C., Pelessone, D., Charman, C.: A coupled fluid/structure modeling of shock interaction with a truck, AIAA-96-0795 (1996)
28. Baum, J.D., Löhner, R., Marquette, T.J., Luo, H.: Numerical simulation of aircraft canopy trajectory, AIAA-97-1885 (1997)
29. Baum, J.D., Luo, H., Mestreau, E., Löhner, R., Pelessone, D., Charman, C.: A coupled CFD/CSD methodology for modeling weapon detonation and fragmentation, AIAA-99-0794 (1999)
30. Ramamurti, R., Sandberg, W., Löhner, R.: Simulation of flow about flapping airfoils using a finite element incompressible flow solver, AIAA-99-0652 (1999)
31. Löhner, R.: Renumbering strategies for unstructured-grid solvers operating on shared-memory, cache-based parallel machines. Comput. Methods Appl. Mech. Eng. **163**, 95–109 (1998). doi:10.1016/S0045-7825(98)00005-X
32. Tuszynski, J., Löhner, R.: Parallelizing the construction of indirect access arrays for shared-memory machines. Commun. Appl. Numer. Methods. Eng. **14**, 773–781 (1998). doi:10.1002/(SICI)1099-0887(199808)14:8<773::AID-CNM186>3.0.CO;2-5
33. Sharov, D., Luo, H., Baum, J.D., Löhner, R.: Implementation of unstructured grid GMRES+LU-SGS method on shared-memory, cache-based parallel computers, AIAA-00-0927 (2000)
34. Löhner, R., Ramamurti, R.: A load balancing algorithm for unstructured grids. Comput. Fluid Dyn. **5**, 39–58 (1995). doi:10.1080/10618569508940735
35. Ramamurti, R., Löhner, R.: A parallel implicit incompressible flow solver using unstructured meshes. Comput. Fluids **5**, 119–132 (1996). doi:10.1016/0045-7930(95)00032-1
36. Löhner, R.: Applied CFD Techniques. Wiley, New York (2001)
37. Lefebvre, M.H., Oran, E.S., Kailasanath, K., Van Tigglelen, P.J.: The influence of the heat capacity and diluent on detonation strucuture. Combust. Flame **95**, 206–218 (1993). doi:10.1016/0010-2180(93)90062-8
38. Yee, H.C.: Upwind and Symmetric Shock-capturing schemes. NASA Tech. Memo. 89464 (1987)
39. Liu, Y., Vinokur, M.: Upwind algorithms for general thermochemical nonequilibrium flows, AIAA-89-0201 (1989)
40. Powers, J.M., Paolucci, S.: Accurate spatial resolution estimates for reactive supersonic flow with detailed chemistry. AIAA J. **43**(5), 1088–1099 (2005). doi:10.2514/1.11641
41. Powers, J.M.: Review of multiscale modeling of detonation. J. Propuls. Power **22**(6), 1217–1229 (2006). doi:10.2514/1.17897
42. Sussman, M.A.: A computational study of unsteady shock-induced combustion of hydrogen–air mixtures, AIAA-1994-3101 (1994)
43. Inaba, K., Matsuo, A.: Cellular structures of planar detonations with a detailed chemical reaction model, AIAA-2001-480 (2001)
44. Gnoffo, P.A., White, J.A.: Computational aerothermodynamic simulation issues on unstructured grids, AIAA-2004-2371 (2004)
45. Delanaye, M., Liu, Y.: Quadratic reconstruction finite volume schemes on 3d arbitary unstructured polyhedral grids, AIAA-99-3259 (1999)
46. Aftosmis, M., Gaitonde, D., Tavares, T.S.: On the accuracy, stability and monotonicity of various reconstruction algorithms for unstructured meshes, AIAA-94-0415 (1994)
47. Pintgen, F., Eckett, C.A., Austin, J.M., Shepherd, J.E.: Direct observations of reaction zone structure in propagating detonations. Combust. Flame **133**, 211–229 (2003). doi:10.1016/S0010-2180(02)00458-3
48. Tsuboi, N., Daimon, Y., Hayashi, A.K.: Three-dimensional numerical simulation of detonations in coaxial tubes. Shock Waves **18**(5), 379–392 (2008). doi:10.1007/s00193-008-0152-z
49. Oran, E.S., Young, T.R., Boris, J.P., Picone, J.M., Edwards, D.H.: A Study of detonation structure: the formation of unreacted gas pockets. Proc. Combust. Inst. **19**, 573–582 (1982)
50. Gamezo, V.N., Desbordes, D., Oran, E.S.: Two-dimensional reactive flow dynamics in cellular detonation waves. Shock Waves **9**, 11–17 (1999). doi:10.1007/s001930050134
51. Watt, S.D., Sharpe, G.J.: Linear and nonlinear dynamics of cylindrically and spherically expanding detonation waves. J. Fluid Mech. **522**, 329–356 (2005). doi:10.1017/S0022112004001946